Energy Conversion and Management: X 22 (2024) 100607

Contents lists available at ScienceDirect

Energy Conversion and Management: X

journal homepage: www.sciencedirect.com/journal/energy-conversion-and-management-x

Operation strategy optimization of an integrated proton exchange membrane water electrolyzer and batch reverse osmosis desalination system powered by offgrid wind energy

Jiong Wang [a], Shanshan Cai [a,b], Ruiyuan Chen [a], Zhengkai Tu [a,b,*], Song Li [a,b,*]

[a] Department of New Energy and Science Engineering, School of Energy and Power Engineering, Huazhong University of Science and Technology, Wuhan 430074, China
[b] China-EU Institute for Clean and Renewable Energy, Huazhong University of Science and Technology, Wuhan 430074, China

ARTICLE INFO

Keywords:
Wind-hydrogen-desalination system
Step-by-step start
Hydrogen production
Fresh water
Switching times

ABSTRACT

Operation strategy of the integrated wind-hydrogen system is the key to ameliorate the negative impacts of the fluctuated wind power on the hydrogen production capacity and durability of electrolyzer. However, the desalination system supplying pure water to electrolyzers was neglected previously, with which the practical operation strategy of the hybrid wind-hydrogen-desalination system has yet to be investigated. In this work, we proposed a novel control strategy named step-by-step start for wind-hydrogen-desalination system consisting of wind turbine, proton exchange membrane water electrolyzer (PEMWE), battery and batch reverse osmosis (BRO) desalination system, which can produce hydrogen and fresh water. Real-time wind data from Shenzhen, China were used as input to the integrated system. The results demonstrate the wind-hydrogen-desalination system with the proposed strategy can improve the hydrogen production by 17.55 %, the energy efficiency by 17.68 % in August, and increase hydrogen production by 10.29 %, the energy utilization efficiency by 10.44 % in December compared with traditional strategies. At low wind speeds, the switching times of PEMWE for this strategy is higher than the other strategies, while at high wind speeds, the switching times of PEMWE is significantly decreased. This work provides insights into the practical operation strategy for wind-hydrogen-desalination system depending on the real-time wind speed.

Nomenclature	
Abbreviations	
PEMWE	Proton exchange membrane water electrolyzer
TDS	Total dissolved solids
N	Number, N = 9
BRO	Batch reverse osmosis
el/EL	Electrolyzer
Symbols	
A	area, (cm^2)
A_m	Active membrane area, (m^2)
A_w	Water permeability, (m/s/Pa)
$a/b/c$	Fitting parameters of wind turbine
B	Salt permeability, (m/s)
C	Concentration, (g/L)
Cap	Battery capacity, (kWh)
d	Diameter, (m)
des	desalination
E	Activation energy, (kJ/mol)

(*continued on next column*)

(*continued*)

Nomenclature	
F	Faraday constant, ($C \cdot mol^{-1}$)
f_{pipe}	Friction factor in the pipe, (-)
f_m	Friction factor inside the RO, (-)
H	Channel height, (m)
i	Ionisation number, (-)
J	Current density, (A/cm^2)
J_W	Permeate flux, ($L/m^2/h$)
L	Length, (m)
$\dot{m}_{H_2}$	Hydrogen product rate, (kg/s)
N	Number, (-)
P	Pressure, (atm)
R	Gas constant,($J \cdot mol^{-1} \cdot K^{-1}$)
R_{PEM}	Ohmic resistance, (Ω)
R_{in}	Internal resistance, (Ω)
S	factor, (-)

(*continued on next page*)

* Corresponding authors at: Department of New Energy and Science Engineering, School of Energy and Power Engineering, Huazhong University of Science and Technology, Wuhan 430074, China.
E-mail addresses: tzklq@hust.edu.cn (Z. Tu), songli@hust.edu.cn (S. Li).

https://doi.org/10.1016/j.ecmx.2024.100607
Received 28 February 2024; Received in revised form 23 April 2024; Accepted 24 April 2024
Available online 26 April 2024
2590-1745/© 2024 The Author(s). Published by Elsevier Ltd. This is an open access article under the CC BY-NC license (http://creativecommons.org/licenses/by-nc/4.0/).

(*continued*)

Nomenclature	
SOC	State of charge, (-)
T	Temperature, (K)
V	Voltage, (V)
V_{pg}	Purged volume, (m^3)
V_{b0}	Work exchanger volume, (m^3)
v	Speed, (m/s)
w	Channel width, (m)
α	Symmetrical factor, (-)
β	Ratio of recirculation flow rate, (-)
σ	Ionic conductivity, (-)
λ	Water content, (-)
η	Efficiency, (-)
δ	Membrane thickness,(μm)
Subscript	
act	Activation
a/c	Anode/Cathode
aux	Auxiliary
bat	Battery
F	Faraday
H_2	Hydrogen
i/j	Serial number
O_2	Oxygen
Li	Lithium
m/mem	Membrane
min	minimum
ip	Inflexion point
mid	Middle
max	Maximum
pre	Pressurization
re	Refill
P/L/R	Polarization/Longitudinal/Retention
oc	Open circuit
ohm	ohmic
r	Rated
ref	Reference
t	total
th	Thermal neutral
v	voltage
0	Initial state

Introduction

With the acceleration of industrialization, mankind's demand for energy is gradually increasing, and the current energy resource is still dominated by fossil fuels. The large amount of fossil fuels consumption has brought about numerous environmental problems, such as global warming and the frequent occurrence of extreme weather [1,2]. The sustainable development goals (SDGs) including the development of clean energy and decarbonisation of energy sources, offering solutions for attaining sustainable development and combating climate change [3,4]. Hydrogen energy is an ideal alternative to fossil fuels due to its abundant source, high calorific value, cleanliness, non-pollution and good environmental friendliness [5]. The intermittent and random nature of renewable energy sources such as solar and wind energy leads to fluctuations in power generation, which will affect the stability of the grid, while the use of off-grid electricity generated from renewable energy sources for electrolysis to produce hydrogen can realize the conversion from unstable solar and wind power to stable chemical energy [6–10]. Hitherto the dominant water electrolysis technologies for hydrogen production are alkaline water electrolysis (AWE), proton exchange membrane water electrolysis (PEMWE), and solid-oxide water electrolysis (SOWE) [11]. Among these approaches, PEMWE is more suitable for hydrogen production coupled with renewable wind and solar energy because of its fast dynamic response and wide power regulation range [12]. In recent years, with the growth of installed capacity of wind turbines, the increasing wind power consumption is expected to avoid its abandonment. Meng et al. [13] developed a model for a wind-hydrogen coupled energy storage power generation system (WHPG), comprising a wind turbine, electrolyzer, fuel cell, compressor, and hydrogen storage tank, and they revealed that surplus electricity in the uncoupled system amounted to approximately 32.6 % of the wind turbine's electricity generation, whereas in the coupled system, it accounted for only about 1.7 % of the wind turbine's electricity generation. Thus, coupling PEMWE with wind turbines can not only decrease the hydrogen production cost but also enhance the energy utilization efficiency.

Wind-powered hydrogen production systems offer a cleaner alternative, significantly reduced carbon emissions compared to traditional methods reliant on coal or natural gas [14,15]. Over recent years, many research efforts have been dedicated to wind-hydrogen system. The study on an on grid wind-hydrogen system composed of a wind farm and PEMWE to generate hydrogen during periods of low electricity price and excess wind energy demonstrated the optimal expected profit surged by 33.42 % when the price of hydrogen increased from DKK 1.2/kWh to DKK 1.8/kWh [16]. Scolaro et al. employed 2017 wind data to simulate the hourly generation of an offshore wind farm in Germany. It is revealed that the most cost-effective system configuration for offshore wind-hydrogen production systems occurs when the electrolyzer capacity is 87 % of the wind farm capacity [17]. Another study using Simulink model of an integrated system comprising 2.3 MW offshore wind turbine and 1.852 MW PEMWE demonstrated the highest hydrogen production was 17,242 kg for 31-day period using real-time wind data and the overall efficiency was in the range 56.1–56.9 % [18]. The impacts of wind power fluctuation on the voltage degradation rate of a 60 kW PEMWE was also investigated based on multi-physics fields three-dimensional model [19], in which the single-stack PEMWE degradation voltage is 7.5 V and the wind-hydrogen system energy efficiency of 61.65 %.

However, the intermittent nature of wind energy is unfavorable for the durability of the system, especially electrolyzers and system efficiency. In order to improve the wind-hydrogen hybrid system performance and lifetime of electrolyzers, effectively coordinating the operation of each component of the system necessitates the implementation of precise operation strategies. These strategies wield a significant impact on hydrogen production, system energy efficiency and the switching times of electrolyzers. To optimize system performance, it is crucial to adopt tailored control strategies for diverse application scenarios. An operational strategy for a ongrid wind-hydrogen-fuel cell system was proposed, in which the power generation was adjusted hourly based on demand utilizing surplus grid electricity for hydrogen generation during periods of low electricity consumption, and generate electricity by fuel cell using the stored hydrogen in tank during periods of high electricity demand. It is found that the conversion efficiency of electricity-hydrogen-to-electricity is about 30 % [20]. Considering the effect of wind speed fluctuation on the operating status of AWE, a segment start strategy is proposed for ongrid wind-electrolyzer-supercapacitor system, the simulation results show that amidst wind fluctuations, the segment start strategy significantly reduces switching times by 93.5 %, and enhances hydrogen production by 44.18 % compared to the simple start-stop strategy [21]. For the wind-hydrogen system involving multiple electrolyzers, operational strategies of the wind power allocation to each electrolyzers is crucial. Zheng proposed a new strategy to allocate wind power to four electrolyzer, which exhibited higher hydrogen production of and energy efficiency of 61.3 % compared with traditional strategies [22]. An optimal scheduling method tailored for a ongrid wind-hydrogen system was proposed based on segmented fuzzy control, which improves hydrogen production efficiency by 4.8 % compared to a conventional simple start-stop scheme [23]. Du et al. [24] proposed an energy management strategy for optimizing an off-grid solar photovoltaic-hydrogen-fuel cell system an electrolyzer, in which the energy efficiency significantly increased from 47.6 % to 53.9 %.

Fresh water is an indispensable raw material for hydrogen production by water electrolyzer, and the feed water for commercial PEMWE requires high purity [25]. Taking into account the limited freshwater resources, it is reasonable to use the abundant seawater for desalination

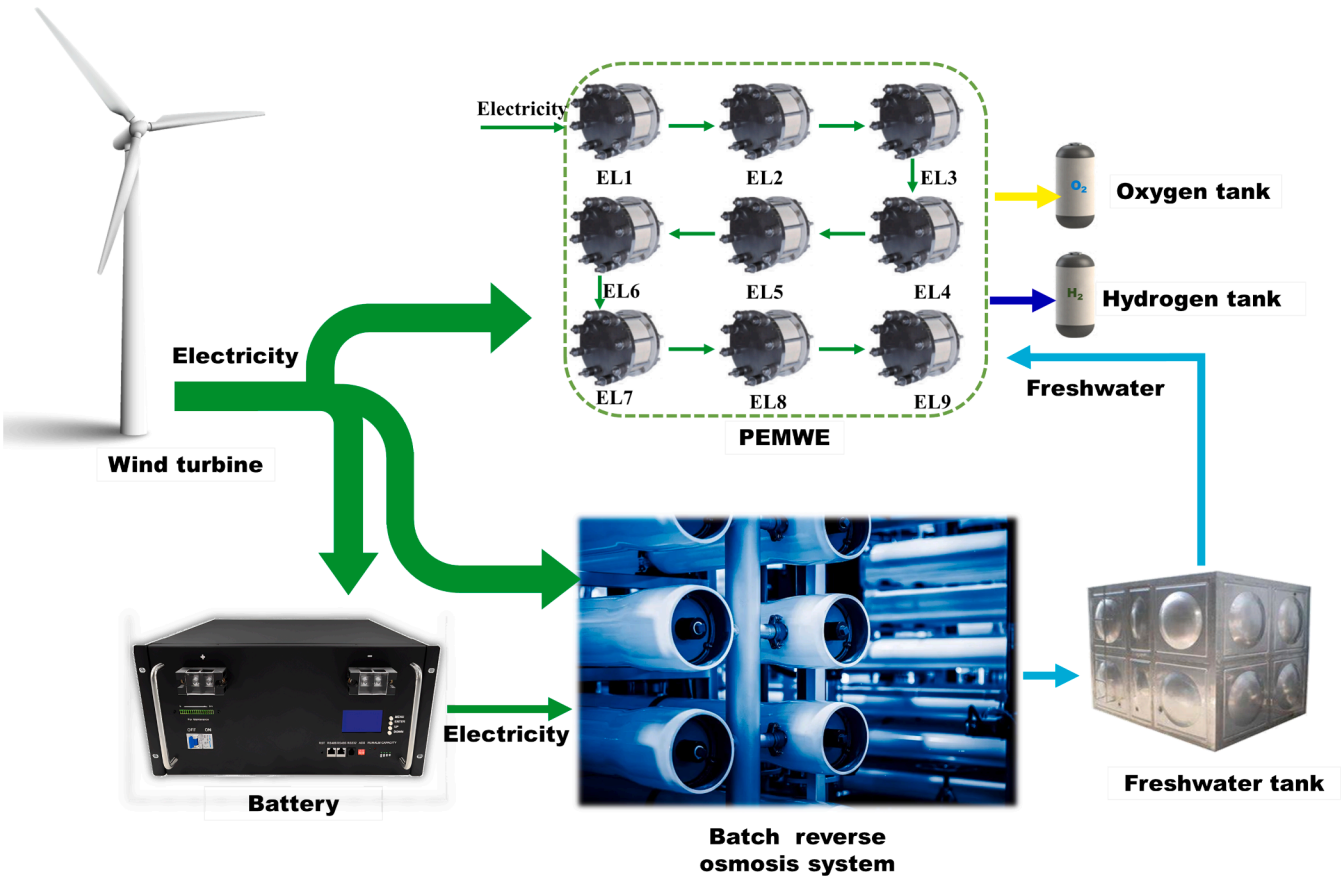

Fig. 1. Schematic of integrated offgrid wind-hydrogen-desalination system.

treatment as a source of feed water for the PEMWE. However, the desalination system for feed water of electrolyzer has not been taken into account in previous hybrid wind-hydrogen systems, and thus the effective operation strategy of the wind-hydrogen-desalination system is the key to guarantee the optimal electricity-hydrogen/water conversion efficiency.

In the context of off-grid wind-hydrogen coupled systems integrated with seawater desalination, this study is focused on operational strategies of the integrated system aiming to reduce electrolyzer switching times to extend their lifespan, enhance hydrogen production, and optimize the energy efficiency of the entire system. The wind-hydrogen coupled system for integrated seawater desalination consists of the wind turbine, PEMWE, seawater desalination system based on the real-time wind data adopted from August and December in Shenzhen city, China as the actual inputs. Section 2 describes the integrated system's components, sizes, and operational principles. Section 3 introduces the models used for the system components. Section 4 presents the three control strategies. By assessing hydrogen production, system energy efficiency, freshwater production, and electrolyzer switching times of three operation strategies based on Simulink model of integrated system, step-by-step start strategy exhibiting enhanced the hydrogen production, high system energy utilization efficiency and smaller switching times of the electrolyzers, is proposed.

System description

System operating principles

The integrated system model in this study was developed using Matlab/Simulink, Fig. 1. The integrated system in Fig. 1 is composed of a 1.5 MW wind turbine, 1.35 MW electrolyzer consisting of nine 150 kW PEMWE stack, a 3 kW batch reverse osmosis (BRO) desalination system, a 600kWh lithium-ion battery, and auxiliary devices including pumps and valves. The contribution of auxiliary devices (like pumps and valves) to overall energy consumption is negligible, hence they were not taken into consideration.

Wind energy is converted into electricity through the wind turbine. BRO system desalinates seawater to produce high-purity fresh water for the PEMWE. It has been demonstrated that utilizing DC power proves notably more efficient as an energy source for electrolysis within electrolyzers compared to AC power [26]. The generated AC power from wind turbine is converted to DC power via an inverter, with an efficiency of 95 %. PEMWE stack convert DC electricity into hydrogen by utilizing high-purity water produced from BRO desalination system. In to eliminate the impacts of wind power fluctuation on operation stability of PEMWE, a lithium-ion battery serves as an energy buffer device, storing surplus wind electricity during optimal power generation periods, which can release stored electricity when generated wind power is low, ensuring stable operation of the PEMWE and BRO system. The produced hydrogen and oxygen are stored separately in dedicated hydrogen and oxygen tanks. Surplus pure water is stored in water tanks, ensuring water self-sufficiency within the overall system.

PEMWE system

As a pivotal element of the wind-hydrogen coupling system, PEMWE primarily transforms electrical energy into a stable form of chemical energy. To augment hydrogen production, multiple electrolyzers are commonly included, classified into series and parallel connections based on their interconnection methods. In a series-connected electrolyzer system, the total electrolytic voltage equals the sum of the voltages across individual electrolyzers, and the currents flowing through each

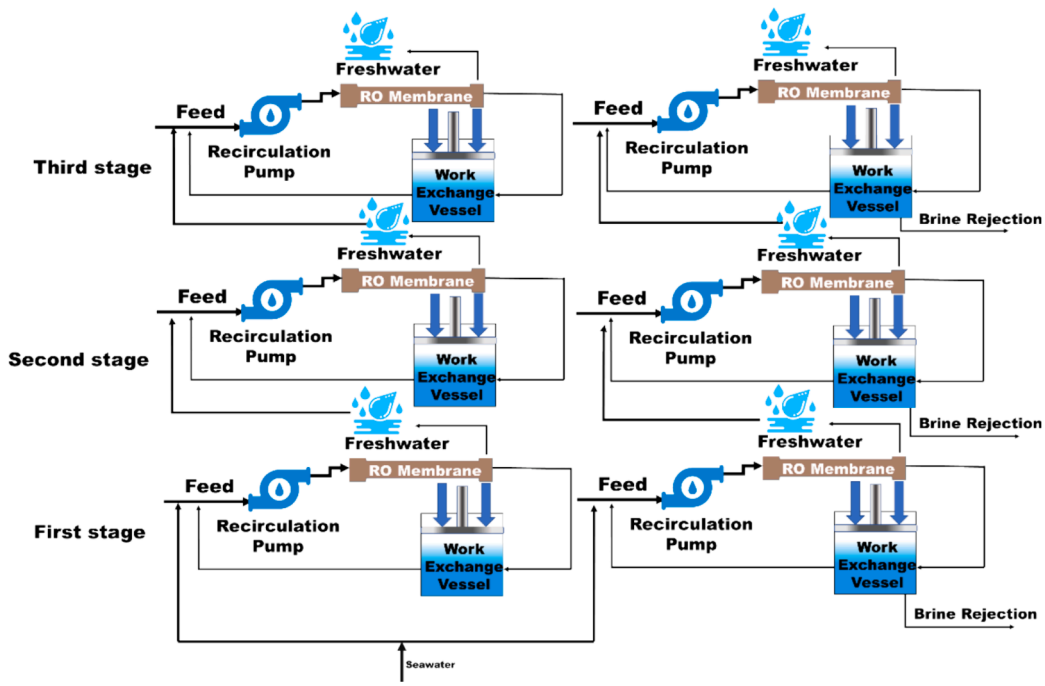

Fig. 2. Three-stage BRO system.

electrolyzer are equal and sum up to the total electrolytic current. Conversely, in a parallel-connected electrolyzer system, the electrolytic current equals the sum of the currents through each electrolyzer, while the voltage across each electrolyzer equals the total voltage. To enhance the compactness of the electrolyzer system and enable operation at higher current densities for improved efficiency and hydrogen production rates, this study employs a series-connected electrolyzer configuration [27]. The startup order of the electrolyzers depends on the instant generated power from wind turbine. As the power generation increases, EL1- EL9 are sequentially activated, allowing for a maximum of nine electrolyzers to start operation.

Four assumptions were made for PEMWE to simplify modelling:

(1) PEMWE maintains a consistent internal temperature without any temperature variations.
(2) The cell voltage includes the energy open-circuit voltage, activation voltage, and ohmic voltage. The impact of diffusion overpotential on the voltage is ignored, as it typically affects the cell voltage only when the current density exceeds 1.6A/cm^2 [28].
(3) Regarding the resistance of the electrolyzer, only the resistance of the proton exchange membrane is taken into account, while disregarding the resistance from the bipolar plates, catalyst layer, and gas diffusion layer.
(4) Consistent pressure is applied to both the anode and cathode.

BRO system

In this study, seawater is desalinated and processed to serve as the feedwater for the electrolyzer by BRO system. Compared with thermal desalination technologies such as multi-stage flash (MSF) and multi-effect distillation (MED), membrane-based desalination technologies such as reverse osmosis (RO) and nano-filtration (NF) techniques exhibit lower energy consumption and facile operation [29]. Compared with RO system, BRO system is more attractive owing to their high yield, minimal energy consumption, high anti-scaling property and outstanding structural resilience. These advantages are particularly pronounced at high recovery rates, which is a crucial goal in various application scenarios such as brackish water desalination. While BRO theoretically boasts higher efficiency compared to continuous RO, it suffers from the drawback that only the pressurization stage yields output [30]. Consequently, when compared with RO, if the output per membrane area remains constant, the permeate water flow rate of BRO will be higher for the intermittent process. However, given the minimal consumption of fresh water in this study, the BRO system is preferred from an energy-saving perspective. Before entering the BRO system, seawater undergoes pre-treatment processes such as flocculation, sedimentation, and filtration to remove insoluble impurities from the seawater. Subsequently, the pre-treated seawater enters the BRO system, where it undergoes the first stage of treatment to separate it into fresh water and brine. The produced freshwater proceeds to subsequent stages for further purification. The brine extracted after the first-stage finds utility in the salt industry. However, the treated freshwater from the second stage cannot be directly applicable in the electrolyzer and requires additional treatment in the third stage to meet the standards for hydrogen electrolysis [31]. Once treated in the third stage, the freshwater satisfies the purity requirement for hydrogen electrolysis. Simultaneously, the brine generated from the second and third treatment stages complies with drinking water standards [32]. Seawater after the first-stage of BRO fails to meet these requirements. Hence, a multi-stage treatment process for seawater is essential. After undergoing a three-stage treatment process, desalinated water can meet the demands of the electrolysis [31]. The layout of the BRO system is depicted in Fig. 2.

The three-stage BRO cycle comprises three processes: pressurization, purge, and refill. During the pressurization, a continuous stream of freshwater is generated, while the purge and refill do not yield freshwater. Each stage of the BRO system in this study comprises two units to maintain an uninterrupted supply of freshwater output.

Simulation model

In this section, the modeling process is thoroughly elucidated. These models are constructed using Matlab/Simulink. Various blocks, including Signal Builder, Matlab Function, Integrator, PID Controller, Constant, Add, Product, Gain, and Out to Workspace, are utilized throughout the modeling process.

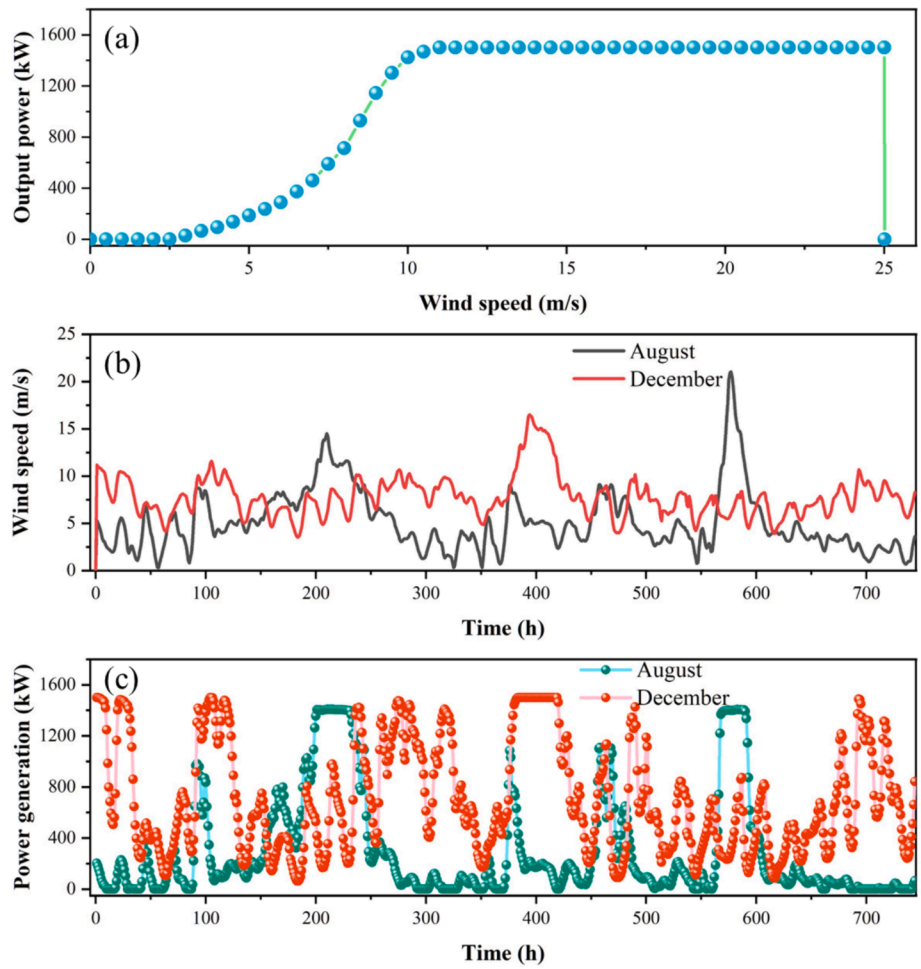

Fig. 3. (a) Power curve of wind turbine, (b) hourly wind speed data across a month, (c) hourly output power across a month.

Table 1
Specific parameters of wind turbine.

Parameter	Value	Parameter	Value	Parameter	Value
P_{rate}	1500	v_{in}/v_{out}	2.5/25	v_r	11
a_1	6.1480×10^3	b_1	0.0303	c_1	−0.1095
a_2	193	b_2	0.8333	c_2	−0.5274
a_3	48.3517	b_3	1.5158	c_3	−0.8680

Wind turbine model

The power generated by a wind turbine is directly related to the wind speed. The wind turbine model used in this study The wind speed and out power relationship is described in Fig. 3(a).

In this study, we established a semi-empirical relationship between wind speed and output power using Fourier fitting based on the parameters provided by the manufacture. The equation between wind speed and output power is can be expressed as:

$$P_{wt} = \begin{cases} 0,\ v < v_{in} \&\& v > v_{out} \\ a_1 \times \sin(b_1 \times v + c_1) + a_2 \times \sin(b_2 \times v + c_2) + a_3 \times \sin(b_3 \times v + c_3),\ v_{in} <= v < v_r \\ P_r, v_r <= v <= v_{out} \end{cases} \quad (1)$$

where P_{wt} represents the power generated by wind turbine, kW; P_r is the rated power of wind turbine, m/s; v is the wind speed, m/s; v_{in} is the cut-in wind speed of wind turbine, m/s; v_r is the rated speed of wind turbine, m/s; v_{out} is the cut-out speed of wind turbine, m/s. a_1, b_1, $c_1 \ldots c_3$ represent the fitted parameters utilized in modeling the power generation of the wind turbine as provided in Table 1. The goodness of fit ($R^{2)}$ of the Flourier model is 99.9 %, indicating a good agreement.

In this study, real-time wind speed data with hourly time steps from Shenzhen City in August and December of 2022 are utilized, sourced from NASA.The temporal variations in wind speed and subsequent power generation demonstrates the low and more erratic wind speeds during the summer and high wind speeds during winter. Notably, the maximum power generation recorded is 1407.8 kW in August and 1500 kW in December. The depicted trend indicates a substantial disparity in power generation between summer and winter.

PEMWE model

The voltage of PEMWE can be described as the sum of open-circuit voltage V_{oc} and two voltage overpotentials of V_{act} and V_{ohm} [33] in Eq. (2):

$$V = V_{oc} + V_{act} + V_{ohm} \tag{2}$$

$$V_{cell} = N_{cell} V \tag{3}$$

where V_{oc} is open-circuit voltage, V_{act} and V_{ohm} are activation overpotential and the ohmic overpotential, respectively. V_{cell} is the voltage of PEMWE, N_{cell} is the number of cells in the electrolyzer stack.

The open-circuit voltage can be expressed below [34]:

$$V_{oc} = 1.23 - 0.9 \times 10^{-3}(T - 298) + 2.3\frac{RT}{4F}\log\left(P_{H_2}^2 P_{O_2}\right) \tag{4}$$

where T is operating temperature of PEMWE (K); R is universal gas constant (8.3145 $Jmol^{-1}K^{-1}$);F is Faraday constant (96,485 $Cmol^{-1}$); P_{H_2} and P_{O_2} are the partial pressures of hydrogen and oxygen, respectively.

The activation overpotential serves as an indicator of the electrodes' activity, depicting the overpotential needed for an electrochemical reaction to occur. This activation overpotential can be described using the Butler-Volmer equation.

$$J = J_{0,i}\left[\exp\left(\frac{\alpha z F \eta_{act,i}}{RT}\right) - \exp\left(\frac{(1-\alpha) z F V_{act,i}}{RT}\right)\right], \mathrm{i} = a, c \tag{5}$$

where J is the current density (A/cm^2), $J_{0,i}$ is exchange current density and subscripts a and c represent anode and cathode, respectively (A/cm^2). α is symmetrical factor and z is the number of electrons involved per reaction. For water electrolysis, α and z are found to be 0.5 and 2, respectively [35]. The activation overpotential of an electrode can be explicitly expressed as:

$$V_{act,i} = \frac{RT}{F}\sinh^{-1}\left(\frac{J}{2J_{0,i}}\right) = \frac{RT}{F}\ln\left[\frac{J}{2J_{0,i}} + \sqrt{\left(\frac{J}{2J_{0,i}}\right)^2 + 1}\right], i = a, c \tag{6}$$

The exchange current density ($J_{0,i}$) indicating the electrode's readiness to proceed with the electrochemical reaction plays a pivotal role in the computation of activation overpotential. High exchange current density suggests high reactivity of the electrode. The exchange current density for PEM electrolysis can be expressed as [36]:

$$J_{0,i} = J_i^{ref}\exp\left(-\frac{E_{act,i}}{RT}\right), \mathrm{i} = a, c \tag{7}$$

where J_i^{ref} is the pre-exponential factor, and $E_{act,i}$ is the activation energy for anode and cathode, respectively.

The ohmic overpotential across the proton exchange membrane results from the membrane's resistance to the movement of hydrogen ions within it. This ionic resistance is influenced by factors such as the humidification degree, membrane thickness, and the temperature at which the membrane operates. The local ionic conductivity $\sigma(x)$ of the membrane has been empirically determined as [37]:

$$\sigma[\lambda(x)] = [0.5139\lambda(x) - 0.326]\exp\left[1268\left(\frac{1}{303} - \frac{1}{T}\right)\right] \tag{8}$$

where x is the location in the membrane measured from the cathode-membrane interface;$\lambda(x)$ is the water content at the location x in the membrane, which can be expressed linearly in terms of water content at the membrane-electrode interfaces:

$$\lambda(\mathrm{x}) = \frac{\lambda_a - \lambda_c}{\delta} + \lambda_c \tag{9}$$

Table 2
Parameters of PEMWE models.

Parameter	Value	Parameter	Value
P_{O_2} (atm)	1.0 [39,40]	J_c^{ref} (A/cm^2)	1.0×10^{-3} [41,42]
P_{H_2} (atm)	1.0 [39,40]	λ_a	14 [37]
T (K)	353	λ_c	10 [37]
$E_{act,a}$ (kJ/mol)	76 [36]	δ(μm)	178
$E_{act,c}$ (kJ/mol)	18 [36]	A_{mem} (cm^2)	900
J_a^{ref} (A/cm^2)	1.0×10^{-9} [41,42]	N_{cell}	40

where δ is membrane thickness (μm), λ_a and λ_c are the water contents at the anode-membrane and cathode-membrane interface, respectively. The total ohmic resistance can be expressed as:

$$R_{PEM} = \int_0^{\delta}\frac{dx}{\sigma[\lambda(x)]} \tag{10}$$

The ohmic overpotential can be expressed in terms of Ohm's law:

$$V_{ohm} = JR_{PEM} \tag{11}$$

The electrical efficiency of the electrolyzer can be calculated by multiplying the Faradaic efficiency and voltage efficiency, formulated as follows:

$$\eta_t = \eta_F \cdot \eta_v \tag{12}$$

The voltage efficiency η_v is defined as:

$$\eta_v = \frac{Vth}{V} = \frac{1.481}{V}[\%]$$

where V_{th} is the thermal neutral voltage, V is a single cell voltage.

The Faradaic efficiency η_F can be calculated as [38]:

$$\eta_F = 96.5\exp\left(\frac{0.09}{JA_{mem}} - \frac{75.5}{(JA_{mem})^2}\right) \tag{13}$$

where A_{mem} is the proton exchange membrane area.

The power consumed by electrolyzer can be calculated as follows:

$$P = E_{cell} J A_{mem} \tag{14}$$

Knowing the power consumption and the efficiency of the electrolyzer allows for the calculation of the hydrogen production rate in Eq. (15):

$$\dot{m}_{H_2} = \frac{P\eta_t}{HHV_{H_2}} \tag{15}$$

where $\dot{m}_{H_2}$ is the hydrogen product rate and HHV_{H_2} is the higher heating value of hydrogen in J/kg.

All parameters of the PEMWE model are provided in Table 2.

BRO model

BRO system comprises three distinct steps of pressurization, purge and refill. During the pressurization, the concentration of the feed solution rises as permeate water consistently exits through the RO membrane module. Therefore, to accommodate this, the applied pressure needs to be augmented throughout the pressurization process. Under the assumption that salt permeation through the RO membrane is negligible, the average applied pressure within the feed pump during the pressurization can be determined using three non-ideal factors as follows [43]:

$$\overline{P}_{p,feed} = S_p S_L S_R \pi_{feed}\frac{1}{r_p}\ln\frac{1}{1-r_p} + \frac{Jw}{Aw} + \frac{\Delta P_m}{2} \tag{16}$$

$$\Delta P_m = \frac{f_m \mu v L}{(0.5H)^2} \tag{17}$$

Table 3
Membrane and operating parameters in BRO model.

Parameter	Value
Water permeability at 25 °C, A_w (m/s/Pa)	3.460×10^{-12}
Salt permeability at 25 °C, B (m/s)	1.210×10^{-8}
Active membrane area, A_m (m^2)	40.800
Concentration polarisation S_P (–)	1.097
Longitudinal concentration gradient S_L (–)	1.044
Salt retention S_R (–)	1.139
Friction factor inside the RO module, fm (–)	20
Length, L (m)	1.020
Inner diameter of the pipes, d_{pipe} (m)	0.02692
Ionisation number, i (–)	1.86480
Channel width, w (m)	40
Purged volume, V_{pg} (m^3)	0.01610
Work exchanger volume, V_{b0} (m^3)	0.06460
Friction factor in the pipe, $fpipe$ (–)	0.03008
Recirculation ratio,β	3.0
Feed pump efficiency, η_{feed} (%)	70
Recirculation pump efficiency, η_{recir} (%)	50
Feed concentration, C_{feed} (g/L)	35
Feed temperature, T_{feed} (oC)	25
Feed flow rate, $\dot{V}_{feed}$(L/h)	10,202
Number of parallel BRO unit (–)	2

$$v = \frac{\dot{V}_{recir} + 0.5\dot{V}_{feed}}{0.5Hw} \tag{18}$$

$$\pi_{feed} = iC_{feed}RT \tag{19}$$

where S_p is the concentration polarization factor, S_L is the longitudinal concentration gradient factor, S_R is the salt retention factor, π_{feed} is the osmotic pressure of the feed solution, r_p is the recovery at pressurization phase, J_W is permeate flux, A_w is the water permeability of the RO membrane, ΔP_m is the pressure drop in the RO membrane module, f_m is the friction factor inside the RO module, L is the RO module length, v is the linear velocity inside the RO module, μ is the solution viscosity, H is the membrane channel height, w is the membrane width, $\dot{V}_{recir}$ is the recirculation flow rate at the exit of the RO module, $\dot{V}_{feed}$ is the feed flow rate, i is the ionisation number, C_{feed} is the feed concentration, R is the gas constant, and T is the temperature.

The peak pressure by the end of the pressurization is described as follows [43]:

$$\widehat{P}_{p,feed} = S_p S_R \pi_{feed} \frac{1}{1 - r_p} + \frac{J_w}{A_w} + \frac{\Delta P_m}{2} \tag{20}$$

The pressure applied by the recirculation pump during the pressurization is determined based on the pressure loss occurring in the RO module and the piping as follows [43]:

$$Pp, recir = \Delta P_m + \frac{\rho}{2}\left(f_{pipe}\frac{L_{pipe,in}v_{pipe,in}^2 + L_{pipe,out}v_{pipe,out}^2}{d_{pipe}} + \sum f_i v_i^2\right) \tag{21}$$

where f_{pipe} represents the friction factor in the pipe, L_{pipe} denotes the pipe length, d_{pipe} signifies the pipe inner diameter. The subscripts *in* and *out* differentiate between the inlet and outlet pipe segments of the RO module. f_i denotes the loss factor in the i`th fitting or valve, calculated via the Darby 3-K method [44]. Additionally, d_{pipe} represent the inner diameters of the pipes. The notation v_i indicates the fluid velocity of the respective pipe or valve.

The permeate concentration during the pressurization is calculated as follows [39]:

$$C_{perm} = \frac{B \cdot A_m}{\dot{V}_{feed}} S_p S_L S_R C_{feed} \frac{1}{r_p} \ln \frac{1}{1 - r_p} \tag{22}$$

where B is the salt permeability of the RO membrane, A_m is the membrane area in the RO module(s) and C_{feed} is the feed concentration.

Table 4
The freshwater production and ion concentration at different stages.

Stage	Freshwater production (m^3/day)	SEC (kWh/m^3)	Ion concentration (kg/m^3)
1st stage	$12.24 \times 2 = 24.48$	2.662	0.1676
2nd stage	$6.12 \times 2 = 12.24$	0.433	5.64×10^{-4}
3rd stage	$3.06 \times 2 = 6.12$	0.221	6.21×10^{-6}

Finally, specific energy consumption (SEC) in the pressurization is calculated [39]:

$$SEC_{pre} = \frac{\overline{P}_{p,feed}}{\eta_{feed}} + \frac{P_{p,recir}\beta}{\eta_{recir}} \tag{23}$$

where β is defined as the ratio of recirculation flow rate at the RO module outlet, η_{feed} and η_{recir} are the feed and recirculation pump efficiency, respectively.

During the purge-and-refill process, the applied pressure in both the feed and recirculation pumps is derived from the pressure drop in the pipes and RO module. Subsequently, the Specific Energy Consumption (SEC) in the purge-and-refill process is calculated as follows [39]:

$$SECre = \frac{P_{r,feed}V_{pg}}{\eta_{feed}V_{b0}} + \frac{P_{r,recir}}{\eta_{recir}} \tag{24}$$

Ultimately, the Specific Energy Consumption (SEC) for the entire process is computed by summing the power consumption, including the SEC of the controller and valve during operation.

$$SEC = SEC_{pre} + SEC_{\mathrm{re}} + SEC_{\mathrm{aux}} \tag{25}$$

The parameters used in the BRO model are summarized in Table 3.

In this work, seawater necessitates successive stages of desalination treatment to attain the requisite ionic concentration for its application as feedwater in the electrolyzer. The study employs a three-stage desalination process for seawater, and the corresponding specific energy consumption and freshwater production are detailed in Table 4.

According to Table 4, the total energy consumption of the BRO system (P_{BRO_0}) is 3.00 kW. The amount of freshwater obtained after the three-stage treatment can fulfill the consumption needs of all electrolyzers operating at maximum capacity. The water resulting from the second-stage treatment, encompassing both freshwater and concentrated brine satisfies the prescribed ion concentration for drinking water. Consequently, the freshwater generated after the second-stage treatment can undergo additional processing to serve as feedwater for hydrogen production in electrolysis tanks. This treated freshwater from the second stage can then be utilized as feedwater for hydrogen production in the electrolyzer. Additionally, the brine produced following the second-stage treatment can find application in various contexts, including irrigation and domestic water use.

Battery model

The state of charge (SOC) is a measure of the proportion of remaining battery capacity relative to the capacity of the fully charged state. To extend the lifespan of lithium battery, SOC was constrained within the range of 0.2 and 0.9 in this study. This limitation aims to optimize the operational conditions of the battery, promoting longevity and preserving its overall health. The SOC can be calculated as follows [45]:

$$SOC = SOC_0 + \frac{1}{C_{ap} \times 3600}\int_{t_0}^{t} I_{Li}(t)\eta_{bat}dt \tag{26}$$

where SOC_0 represents the SOC of the battery at the initial moment, which is set to 0.3; C_{ap} is the maximum battery capacity, which is set to 600kWh; I_{Li} is the working current of battery. Positive values denote the battery being in a state of discharge, while negative values indicate a state of charge.η_{bat} represents the Coulombic efficiency, which is set to

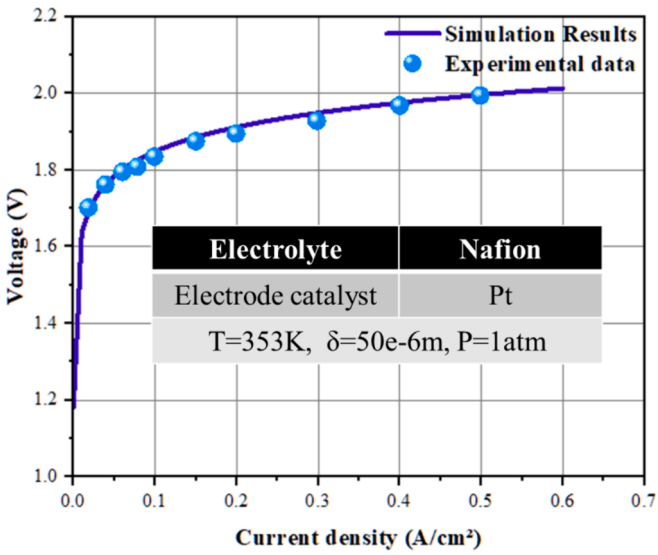

Fig. 4. Model validation of PEMWE.

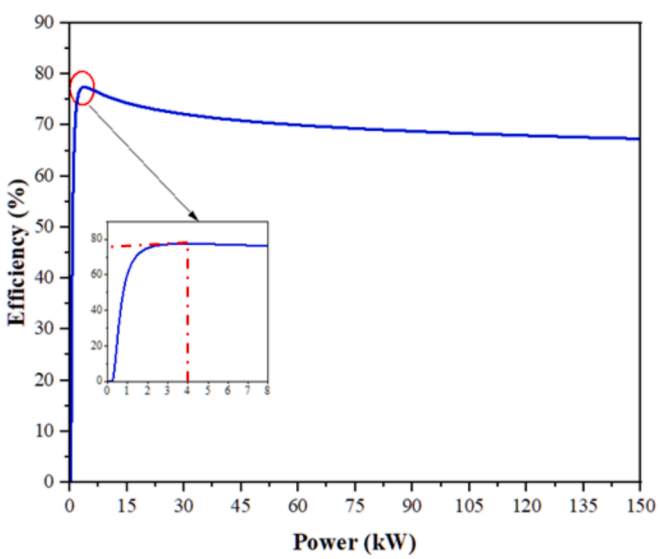

Fig. 5. The relationship between hydrogen production efficiency and input power.

0.95.

The battery voltage is determined as the disparity between the open-circuit voltage and the voltage generated from the internal resistance. This relationship is articulated by the following equation:

$$V_{Li} = V_{oc} - R_{in} I_{Li} \tag{27}$$

The open-circuit voltage and internal resistance of the battery are contingent upon SOC of the battery, as represented by the following equations [46]:

$$Voc = 3.685 - 1.031e^{-35SOC} + 0.2156SOC - 0.1178SOC^2 + 0.3201SOC^3 \tag{28}$$

$$R_{in} = 0.1562e^{-24.37SOC} + 0.07446 \tag{29}$$

where V_{oc} is the open-circuit voltage of battery, R_{in} is the internal resistance.

Model validation

The models of BRO [39] and lithium ion battery [46] systems in this work have been validated in previous study. The PEMWE model is validated as shown in the Fig. 4. The maximum error between the simulated results of the PEMWE and the experimental data [40] is less than 1 %, indicating a high level of accuracy, further confirming the precision and reliability of the mathematical model utilized in this study.

Control strategy of integrated system

The wind-hydrogen coupled energy system can be categorized into two types: grid-connected and off-grid systems. Absolutely, the primary objective of a grid-connected wind-hydrogen coupling system revolves around minimizing wind power wastage, harnessing surplus wind energy for hydrogen production, and enhancing overall energy efficiency. Conversely, off-grid wind-hydrogen coupling systems predominantly concentrate on hydrogen production. In this study, the primary emphasis is placed on analyzing off-grid wind-hydrogen coupling systems. In this study, the correlation between the total efficiency of the electrolyzer and its power is established based on the PEMWE model as illustrated in Fig. 5. The graph demonstrates an initial rise in the electrolyzer's efficiency with increasing operational power, followed by a decline after reaching a peak, particularly noticeable around the power of 4 kW ($P_{el,min}$).

Consequently, adopting a strategy that involves commencing the electrolyzer at lower power levels during low generating power, gradually scaling up the electrolyzer's power as the generating power increases (effectively grading the electrolyzer's power range), proves beneficial [19]. This approach aids in augmenting hydrogen production and, subsequently, elevating the overall system efficiency.

Energy management strategies wield substantial influence over hydrogen production, energy efficiency, and the operational switching times of the electrolyzer within wind-hydrogen coupled systems. Hence, customized energy management strategies are imperative for diverse application scenarios to enhance the performance of integrated system. Considering the relationship between electrolyzer input power and hydrogen production efficiency in Fig. 5, the flow diagram of the step-by-step start strategy outlining the integrated system is depicted in Fig. 6. This illustration embodies the orchestrated management of energy resources to optimize system performance.

As illustrated in Fig. 6, the electricity generated from the battery or the wind turbine takes precedence in catering to the consumption needs of the desalination system. This prioritization ensures that the electrolyzes operate without constraints of freshwater availability. The freshwater production in the desalination system is determined by the freshwater consumption of all electrolyzers operating at their maximum capacity.

Step-by-step start strategy: each electrolyzer (EL1, EL2, …, EL9) is divided into three stages based on its operational power. Parameters i and j represent the numerical sequence from 1 to 9 for these electrolyzers. The electricity generated by the wind turbine is initially allocated to meet the energy demands of BRO system, ensuring an adequate production of fresh water. If the power is consumed by the electrolyzers, $P_{EL} > 0 (P_{EL} = P_{wind}\text{-}P_{des})$, the desalination system operates at its rated power. Otherwise, the operation of desalination system depends on SOC of battery: if SOC is greater than 0.2, the desalination system operates at its rated power; otherwise, it shuts down. The sequence of events is as follows:

(1) If the total power allocated to the electrolyzers $P_{EL} < 0$, all electrolyzers are deactivated. In such instances, if the SOC of battery surpasses 0.2, they provide power to the BRO system. Otherwise, the desalination system shuts down, and the electricity from the wind turbine recharges the batteries.

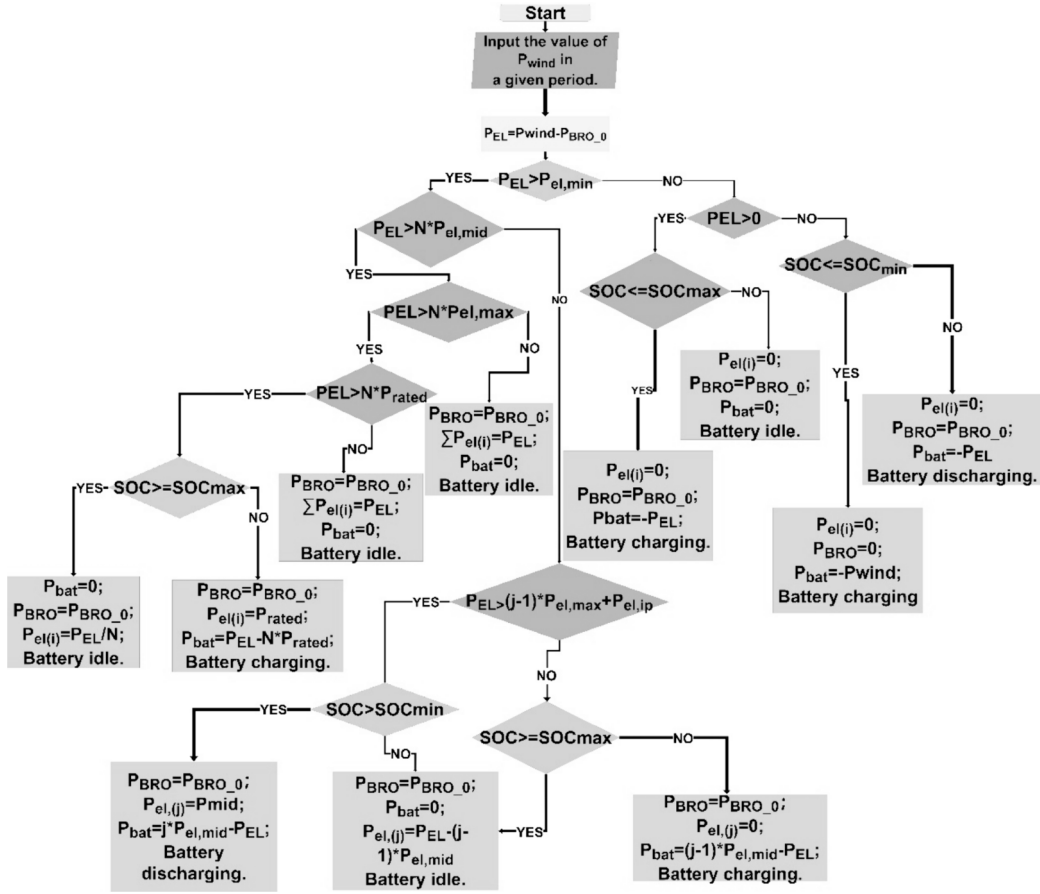

Fig. 6. The step-by-step start control strategy of integrated system.

(2) If P_{EL} below the minimum starting power, $P_{el,min}$, the electrolyzer shuts down. Simultaneously, if the SOC exceeds 0.9, battery is in an idle state; otherwise, it is charged. When P_{EL} exceeds $P_{el,min}$, EL1 initiates operation, and $P_{el,min}$ is 10 % of the rated power.

(3) As P_{EL} surpasses $P_{el,mid}$ (i.e. 50 % of P_{rated}) and extends beyond P_{ip} (set at 4 kW), EL2 activates to utilize the excess wind energy. If the SOC exceeds 0.2, the battery provides power to EL2 up to P_{mid}; otherwise, the battery is idle. The equation $P_{el(2)} = P_{EL}\text{-}P_{el,mid}$ governs EL2′s power consumption. When P_{EL} exceeds the $P_{el,mid}$ of EL2, any additional power is allocated to EL3, and this pattern persists until all electrolyzers are initiated, completing the first stage of startup.

(4) As P_{EL} rises, surpassing the value of $P_{el,max}$ designated for each electrolyzer (i.e., 80 % of the P_{rated}), the startup advances to the second stage, during which the battery ceases to provide power to electrolyzers.

(5) If P_{EL} continues to rise, the surplus power is initially directed to EL1 to reach its rated power. Then, it extends to EL2, EL3, and so forth until all electrolyzers. During this phase, the battery remains inactive. When $P_{EL} > 9P_{rated}$, all electrolyzers operate at their rated power. If the SOC falls below 0.9, it is charged. However, if SOC $\geq$ 0.9, the battery stops charging. In rare instances, when there is an excess of power beyond this point, it is allocated to the electrolyzers. This systematic approach ensures a staged and organized startup of the electrolyzers based on the available wind power.

Two conventional strategies including simple start-stop strategy and slow start strategy were also implemented as control.

Simple start-stop strategy: EL1 initiates operation when the power of all electrolyzers (P_{EL}) exceeds the individual rated power (P_{rated}) for each electrolyzer. As P_{EL} continues to rise and reaches the P_{rated} of EL2, EL2 commences its operation. This sequential activation continues, with each successive electrolyzer being started as the total power matches the power rating designated for each one.

Slow start strategy: Each electrolyzer has its minimum starting power $P_{el,min}$.EL1 initiates its operation when the total power (P_{EL}) surpasses the minimum starting power $P_{el,min}$. As P_{EL} continues to rise, EL1′s output power increases accordingly. Upon further escalation of P_{EL}, if it exceeds the rated power of EL1 and $P_{el,min}$ of EL2, EL2 starts operating while EL1 functions at its rated power. This pattern of gradual activation continues for subsequent electrolyzers in a similar sequential manner.

Based on the aforementioned strategies and the relationship between the starting power of the electrolyzer and efficiency illustrated in Fig. 5, we can determine the efficiency of the electrolyzer under the three strategies. The efficiency of the electrolyzer varies depending on the minimum starting power under different control strategies. With the smallest minimum starting power in the step-by-step start strategy, the electrolyzer's efficiency ranges from 66.84 % to 73.25 %. In contrast, the minimum starting power falls in the middle for the slow start strategy, resulting in the electrolyzer's efficiency varying from 66.84 % to 71.6 %. Conversely, the simple start-stop strategy initiates the electrolyzer only at the rated power, maintaining a consistent efficiency of 66.84 %.

Results and discussion

The proposed integrated system in this study comprises a 1.5 MW wind turbine, a 3 kW BRO seawater desalination system, nine proton exchange membrane electrolyzers with a total capacity of 1.35 MW, and 600 kWh lithium batteries. Simulations of the system were conducted using the wind speeds recorded in Shenzhen City for August and

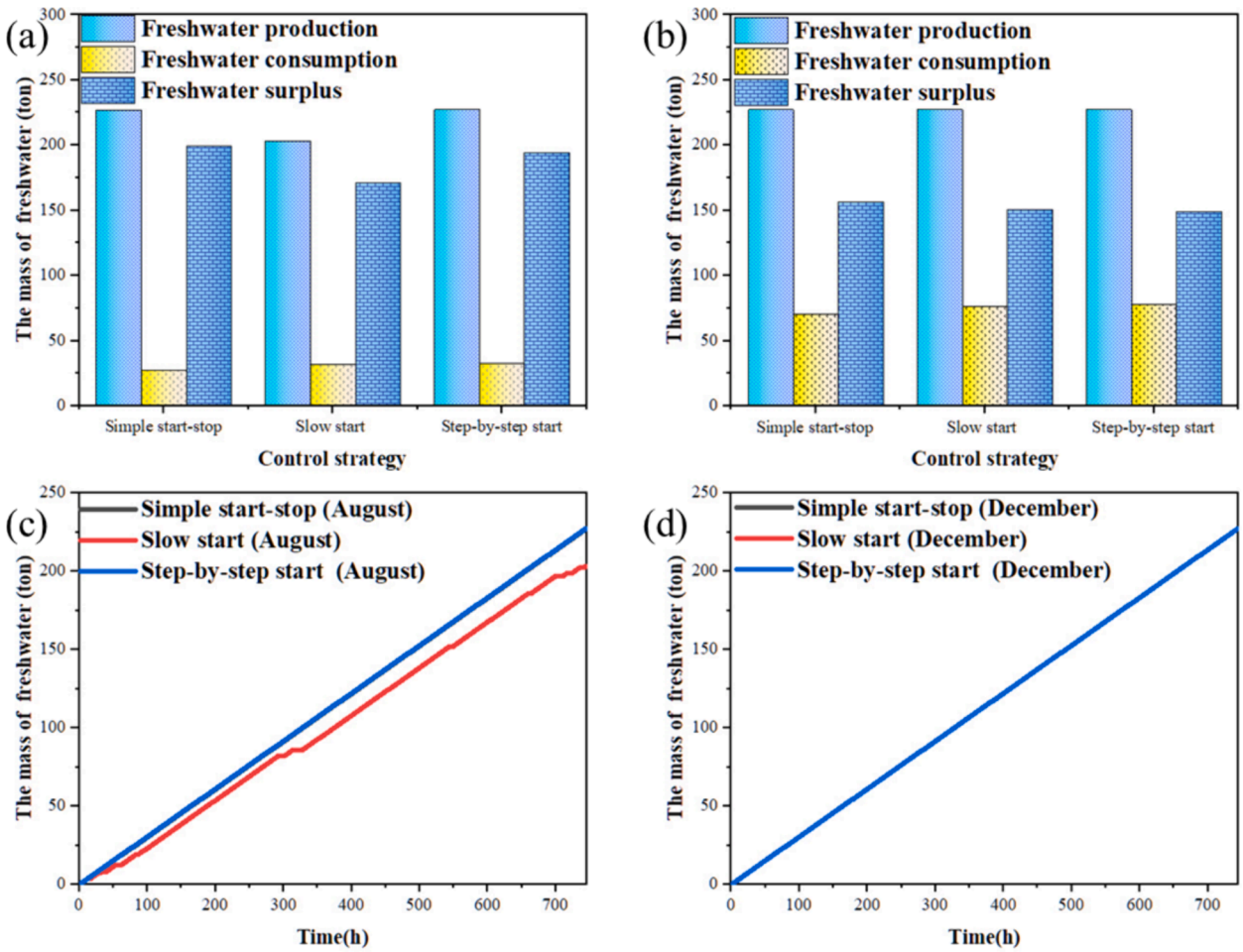

Fig. 7. (a) Freshwater production and consumption (August), (b) freshwater production and consumption (December), (c) freshwater production for the whole month of August (in hours), (d) freshwater production for the whole month of December (in hours).

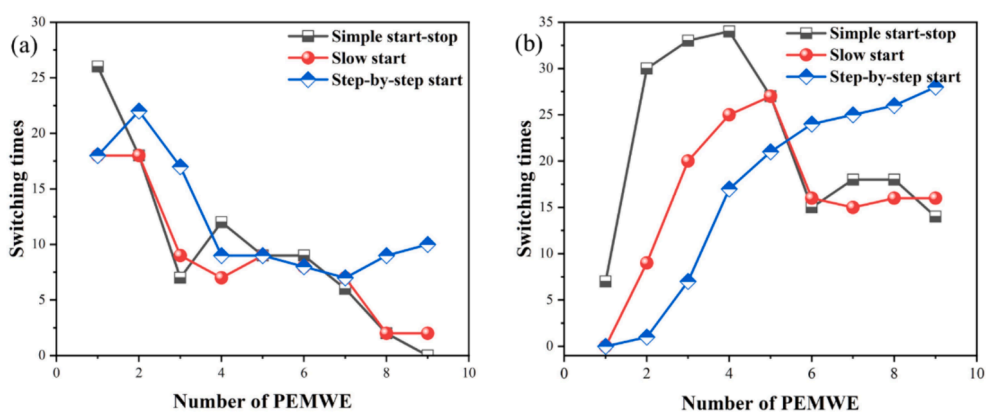

Fig. 8. Switching times of each PEMWE. (a) August (b) December.

December as input parameters, employing the control strategy outlined in Section 4.

Fig. 7 illustrates the freshwater production and consumption of the integrated system by different strategies, primarily linked to wind turbine and lithium battery power. When wind turbine power is absent, the lithium battery takes over. If the SOC of lithium battery drops below 0.2, the desalination system shuts down, ensuring enough water for hydrogen production in the electrolyzer. Freshwater consumption aligns with hydrogen production rates—higher rates favor increased freshwater usage. In August, freshwater production across three strategies varied: 227.0 tons, 203.4 tons, and 227.4 tons, with the slow-start strategy yielding the least. However, by December, all three strategies showed almost identical freshwater production. Low wind speeds in August led to wind power primarily used for water electrolysis, causing longer desalination system downtimes due to low lithium battery SOC, which results a reduction in the freshwater yield of the integrated system using the two traditional strategies.

Figs. 7c and d illustrate the variations in freshwater production during August and December, respectively. In Fig. 7c, intermittent levels of the freshwater output line, indicative of the slow-start strategy,

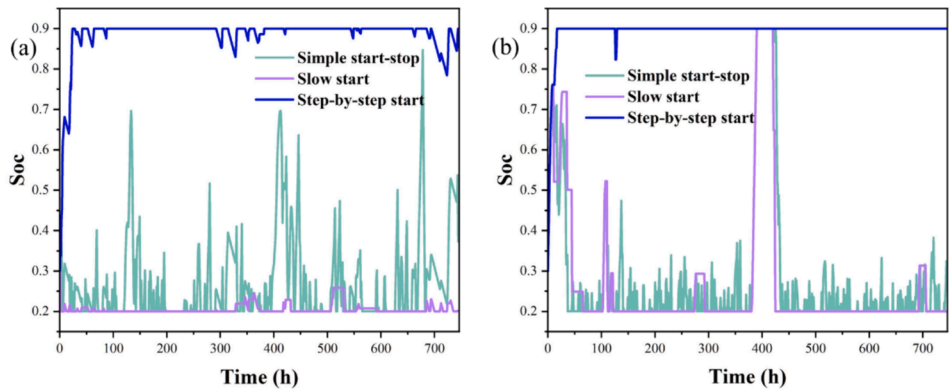

Fig. 9. SOC of battery (a) August (b) December.

denote periods when the desalination system was inactive, halting freshwater production. While the identical in freshwater output for the simple start-stop and step-by-step start strategies throughout August in Fig. 7c owing to the continuing operation of BRO system for freshwater production. Conversely, Fig. 7d exhibits a consistent freshwater yield across the integrated system for the three strategies during December, which results from the uninterrupted operation of the desalination system at its rated power.

Fig. 8 illustrates the comparative relationship among the switching times of each electrolyzer. In August, the total switching times for the three control strategies were as follows: 89 times for the simple start-stop, 80 times for the slow start, and 109 times for the step-by-step start. This indicates an increase in the total switching times of electrolyzers when using the newly proposed control strategy compared to the two traditional ones. The rationale behind this lies in the lower wind power and significant wind speed fluctuations during August. The newly proposed strategy initiates more electrolyzers at lower power levels, thus leading to increased switching times when wind speeds decrease. This observation is reinforced by the notably higher switching frequency of the front-numbered electrolyzers compared to the back-numbered ones.

The total switch times in December across the three control strategies stands at 196 for simple start-stop, 144 for slow start, and 149 for step-by-step start. There is a decreased switch times in the step-by-step start strategy compared to simple start-stop and a slight increase compared with slow start. The switching times for electrolyzers under traditional strategies fluctuates with the number of electrolyzer involved, peaking midway and then gradually decreasing. Conversely, under the new strategy, the switching times steadily increases with the rising number of electrolyzers. This trend emerges because wind power generation is concentrated between 300 and 800 kW, causing frequent start/stops for EL3-EL5 in the two traditional strategies. However, under step-by-step start strategy, the electrolyzers start gradually from EL1 to EL9. Fluctuations in generation power influence the subsequent electrolyzer start/stop times, presenting a similar trend, albeit without a significant increase in the total switch times.

The lithium battery serves a crucial role in energy regulation within the system and its SOC alters over time, depicted in Fig. 9. Notably, the SOC status differs significantly across the three operation strategies. Specifically, the SOC remains stable at 0.9 under the step-by-step start strategy, whereas it continuously fluctuates under the other two strategies, oscillating up and down without stabilization. Under the traditional strategies, the lithium battery intervenes frequently in the system, engaging in repeated charging and discharging cycles to power both the electrolyzer and the desalination system. Conversely, the step-by-step strategy showcases smoother operation of the lithium battery. Even during August's erratic wind fluctuations, it primarily supplies power to the desalination system to sustain the wind generator's normal operation during shutdowns.

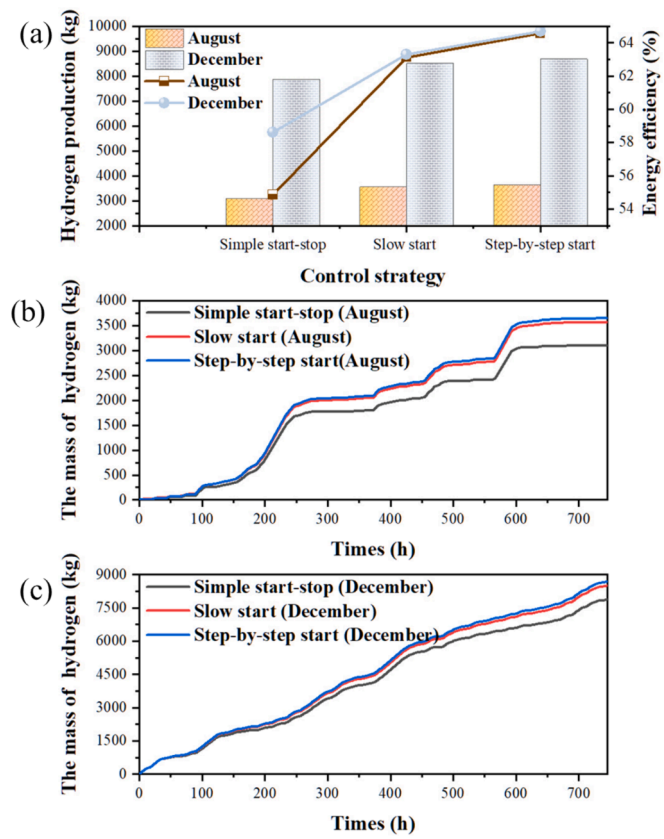

Fig. 10. (a) Hydrogen production and energy efficiency (The bar graph illustrates hydrogen production, while the dotted line graph depicts the energy utilization efficiency of the integrated system), (b) The real-time hydrogen production throughout August (measured in hours), (c) The real-time hydrogen production throughout December (measured in hours).

After one month's operation, the SOC of August were 0.37 for simple start-stop strategy, 0.20 for slow start strategy, and 0.90 for step-by-step start strategy, with only the slow start strategy showing discharge while the rest charging. In December, SOCs were 0.32 for simple start-stop strategy, 0.2 for slow start strategy, and 0.9 for step-by-step start strategy, with only the slow-start battery discharging and the others charging. Frequent charge–discharge cycles are not beneficial for battery health, emphasizing the advantage of the step-by-step start strategy in maintaining good battery condition.

Beyond comparing the integrated system's component operations, assessing the system's energy management strategy crucially involves evaluating its hydrogen yield and energy utilization efficiency, both

Table 5
Performance of the wind-hydrogen-desalination system under three control strategies.

Month	Control strategy	Hydrogen production (kg)	Freshwater production (ton)	Freshwater consumption (ton)	Average SOC	Energy efficiency (%)	Total switching times of electrolyzers (per month)
August	Simple start-stop	3097	227.07	27.87	0.37	54.87	89
	Slow start	3564.4	203.37	32.08	0.20	63.13	80
	Step-by-step start	3640.6	227.38	32.77	0.90	64.57	109
December	Simple start-stop	7884.7	227.38	70.96	0.32	58.62	196
	Slow start	8514.6	227.38	76.63	0.20	63.29	144
	Step-by-step start	8696.3	227.38	78.27	0.90	64.68	149

illustrated in Fig. 10 across the three control strategies. It is revealed that hydrogen production and energy efficiency are at their lowest with the simple start-stop strategy, while they peak with the step-by-step start strategy. The slow start strategy positions hydrogen production and energy utilization efficiency between the two. Notably, compared to the simple start-stop strategy, the slow start strategy shows more significant improvement. The step-by-step start strategy demonstrates a 17.55 % and 2.14 % increase in hydrogen production amount in August and a 10.29 % and 2.14 % increase in December. Meanwhile, the energy utilization efficiency of the integrated system operating under the step-by-step start strategy fluctuates between 64.48 % and 64.57 %, which is significantly higher than the system comprising 2.3 MW offshore wind turbine and 1.852 MW PEMWE (56.1–56.9 %) [18]. Compared to the two conventional control strategies in this work, there is a 17.68 % and 2.28 % increase in the energy utilization efficiency for August and a 10.44 % and 2.20 % increase for December, respectively.

Figs. 10b and 10c illustrate the real-time hydrogen production for three strategies during August and December, respectively. It is found that throughout August, due to low and unstable wind speeds, only a number of the nine electrolyzers could operate, resulting in inconsistent power generation from the wind turbine. In December (Fig.10c), high wind speeds led to increased power generation by the wind turbine. Consequently, hydrogen production continued to rise, with rare appearances of horizontal lines indicating electrolyzer shutdowns. Within the initial 200 h, minimal disparity in hydrogen production was observed among the integrated system utilizing the three strategies. However, beyond the 200 h, the step-by-step start strategy facilitated the initiation of more electrolyzers. This approach enhanced the hydrogen production efficiency of each electrolyzer (Fig. 5), leading to an overall augmentation in hydrogen generation. Consequently, the system employing the step-by-step start strategy gradually surpassed the other two strategies over time.

In summary, the hybrid system employing the step-by-step strategy demonstrated significant improvements in both hydrogen yield and energy efficiency compared to the conventional simple start-stop and slow start strategies. This improvement was found to be positively correlated with their freshwater consumption, as detailed in Table 5. While the freshwater yields among the three strategies were comparable except the slow-start strategy in August, which is ascribed to the failure to initiate the BRO due to insufficient battery power (SOC $\leq$ 0.2) at ultralow wind speed. SOC of battery followed the order of step-by-step start > simple start-stop > slow-start, which is mainly contributed by the higher charging opportunity for step-by-step start strategy. The step-by-step start strategy has the highest number of switching times in August, attributed to the low and fluctuating summer wind speeds, which increased the switching probability of electrolyzers. In contrast, although the switching times for all three strategies increased in December compared to August, the switching times of step-by-step start strategy is relatively lower than simple start-stop, which is primarily ascribed to the operating state of the electrolyzers after the second stage of the step-by-step start strategy. The low operating power of the electrolyzers imposed insignificant impact on the switching times of electrolyzers unless there was a drastic short-term variation in wind speed of summer, which favors the reduced number of switching times in the step-by-step start strategy.

Conclusions and future work

In this study, we established an integrated model of a wind-hydrogen-desalination system powered by fluctuating wind energy to produce hydrogen and fresh water. A novel operation strategy for the hybrid system at two operational scenarios, low-wind-speed summer and high-wind-speed winter, has been proposed to improve hydrogen production and energy efficiency. Using wind data from August and December in Shenzhen City as a case study, the integrated system employing the step-by-step start strategy yields hydrogen production of 3640.6 kg and 8693 kg in August and December, respectively. Compared to the slow start and simple start-stop strategies, the step-by-step start strategy gives rise to an increase in hydrogen production of 17.55 % and 2.14 % in August, and 10.29 % and 2.14 % in December, respectively. Additionally, the energy utilization efficiencies of the step-by-step start strategy are 64.48 % and 64.57 %, respectively, demonstrating improvements of 17.68 % and 2.28 % in August, and 10.44 % and 2.20 % in December, respectively, compared with the two conventional operation strategies. Moreover, regardless of an increase in electrolyzer switching times during low-wind-speed summer, step-by-step start strategy demonstrates enhanced hydrogen production, increased energy utilization efficiency and reduced switching times in high-wind-speed winter, contributing to the stable operation of the system. It should be noted the findings from this work may be further validated in real-world scenarios beyond the constraints and simplifications of simulations. Besides, the thermal management of the PEMWE electrolyzer and the heat source for heating fresh water were not taken into account in this study. This omission could potentially result in an overestimation of the system's energy efficiency, highlighting the need for further investigation in future research endeavors.

CRediT authorship contribution statement

Jiong Wang: Writing – original draft, Visualization, Investigation, Data curation. **Shanshan Cai:** Writing – review & editing, Validation, Investigation, Formal analysis, Conceptualization. **Ruiyuan Chen:** Writing – original draft, Visualization, Investigation, Data curation. **Zhengkai Tu:** Writing – review & editing, Supervision, Resources, Project administration, Methodology, Conceptualization. **Song Li:** Writing – review & editing, Supervision, Resources, Project administration, Methodology, Funding acquisition, Data curation, Conceptualization.

Declaration of competing interest

The authors declare that they have no known competing financial interests or personal relationships that could have appeared to influence the work reported in this paper.

Data availability

Data will be made available on request.

Acknowledgments

This work was supported by National Key Research and Development Program (No. 2022YFB4003704).

References

[1] Lund H. Renewable energy strategies for sustainable development. Third Dubrov Conf Sustain Dev Energy Water Environ Syst 2007;32:912–9. https://doi.org/10.1016/j.energy.2006.10.017.
[2] Jani A, Karimi H, Jadid S. Two-layer stochastic day-ahead and real-time energy management of networked microgrids considering integration of renewable energy resources. Appl Energy 2022;323:119630. https://doi.org/10.1016/j.apenergy.2022.119630.
[3] Olabi AG, Abdelkareem MA, Mahmoud MS, Elsaid K, Obaideen K, Rezk H, et al. Green hydrogen: Pathways, roadmap, and role in achieving sustainable development goals. Process Saf Environ Prot 2023;177:664–87. https://doi.org/10.1016/j.psep.2023.06.069.
[4] Jovan DJ, Dolanc G, Pregelj B. Cogeneration of green hydrogen in a cascade hydropower plant. Energy Convers Manag X 2021;10:100081. https://doi.org/10.1016/j.ecmx.2021.100081.
[5] Ibrahim H, Ilinca A, Perron J. Energy storage systems—Characteristics and comparisons. Renew Sustain Energy Rev 2008;12:1221–50. https://doi.org/10.1016/j.rser.2007.01.023.
[6] Panwar NL, Kaushik SC, Kothari S. Role of renewable energy sources in environmental protection: A review. Renew Sustain Energy Rev 2011;15:1513–24. https://doi.org/10.1016/j.rser.2010.11.037.
[7] Yang Y, Bremner S, Menictas C, Kay M. Forecasting error processing techniques and frequency domain decomposition for forecasting error compensation and renewable energy firming in hybrid systems. Appl Energy 2022;313:118748. https://doi.org/10.1016/j.apenergy.2022.118748.
[8] Sutherland PE. Ensuring stable operation with grid codes: A look at Canadian wind farm interconnections. IEEE Ind Appl Mag 2016;22:60–7. https://doi.org/10.1109/MIAS.2015.2459105.
[9] Mohseni-Bonab SM, Rabiee A, Mohammadi-Ivatloo B. Voltage stability constrained multi-objective optimal reactive power dispatch under load and wind power uncertainties: A stochastic approach. Renew Energy 2016;85:598–609. https://doi.org/10.1016/j.renene.2015.07.021.
[10] Mehrpooya M, Rahbari C, Moosavian SMA. Introducing a hybrid multi-generation fuel cell system, hydrogen production and cryogenic CO2 capturing process. Chem Eng Process - Process Intensif 2017;120:134–47. https://doi.org/10.1016/j.cep.2017.07.008.
[11] Anwar S, Khan F, Zhang Y, Djire A. Recent development in electrocatalysts for hydrogen production through water electrolysis. Int J Hydrog Energy 2021;46:32284–317. https://doi.org/10.1016/j.ijhydene.2021.06.191.
[12] Ganjehsarabi H. Performance assessment of solar-powered high pressure proton exchange membrane electrolyzer: A case study for Erzincan. Int J Hydrog Energy 2019;44:9701–7. https://doi.org/10.1016/j.ijhydene.2018.12.007.
[13] Meng Z, He Q, Shi X, Cao D, Du D. Research on energy utilization of wind-hydrogen coupled energy storage power generation system. Sep Purif Technol 2023;313:123439. https://doi.org/10.1016/j.seppur.2023.123439.
[14] Ramakrishnan S, Delpisheh M, Convery C, Niblett D, Vinothkannan M, Mamlouk M. Offshore green hydrogen production from wind energy: Critical review and perspective. Renew Sustain Energy Rev 2024;195:114320. https://doi.org/10.1016/j.rser.2024.114320.
[15] Robust Multi-objective optimal dispatching model for a novel island micro energy grid incorporating biomass waste energy conversion system, desalination and power-to-hydrogen devices, Appl Energy, 2023;343:121176. https://doi.org/10.1016/j.apenergy.2023.121176.
[16] Xiao P, Hu W, Xu X, Liu W, Huang Q, Chen Z. Optimal operation of a wind-electrolytic hydrogen storage system in the electricity/hydrogen markets. Int J Hydrog Energy 2020;45:24412–23. https://doi.org/10.1016/j.ijhydene.2020.06.302.
[17] Scolaro M, Kittner N. Optimizing hybrid offshore wind farms for cost-competitive hydrogen production in Germany. Int J Hydrog Energy 2022;47:6478–93. https://doi.org/10.1016/j.ijhydene.2021.12.062.
[18] Egeland-Eriksen T, Jensen JF, Ulleberg Ø, Sartori S. Simulating offshore hydrogen production via PEM electrolysis using real power production data from a 2.3 MW floating offshore wind turbine. Int J Hydrog Energy 2023;48:28712–32. https://doi.org/10.1016/j.ijhydene.2023.03.471.
[19] Lu X, Du B, Zhou S, Zhu W, Li Y, Yang Y, et al. Optimization of power allocation for wind-hydrogen system multi-stack PEM water electrolyzer considering degradation conditions. Int J Hydrog Energy 2023;48:5850–72. https://doi.org/10.1016/j.ijhydene.2022.11.092.
[20] Bernal-Agustín JL, Dufo-López R. Hourly energy management for grid-connected wind–hydrogen systems. Int J Hydrog Energy 2008;33:6401–13. https://doi.org/10.1016/j.ijhydene.2008.08.026.
[21] Fang R, Liang Y. Control strategy of electrolyzer in a wind-hydrogen system considering the constraints of switching times. Int J Hydrog Energy 2019;44:25104–11. https://doi.org/10.1016/j.ijhydene.2019.03.033.
[22] Zheng Y, Huang C, Tan J, You S, Zong Y, Træholt C. Off-grid wind/hydrogen systems with multi-electrolyzers: Optimized operational strategies. Energy Convers Manag 2023;295:117622. https://doi.org/10.1016/j.enconman.2023.117622.
[23] Hong Z, Wei Z, Han X. Optimization scheduling control strategy of wind-hydrogen system considering hydrogen production efficiency. J Energy Storage 2022;47:103609. https://doi.org/10.1016/j.est.2021.103609.
[24] Du B, Zhu S, Zhu W, Lu X, Li Y, Xie C, et al. Energy management and performance analysis of an off-grid integrated hydrogen energy utilization system. Energy Convers Manag 2024;299:117871. https://doi.org/10.1016/j.enconman.2023.117871.
[25] Ginsberg M, Zhang Z, Atia A, Venkatraman M, Esposito D, Fthenakis V. Integrating Solar Energy, Desalination and Electrolysis. Sol RRL 2021;6. https://doi.org/10.1002/solr.202100732.
[26] Stansberry J, Hormaza Mejia A, Zhao L, Brouwer J. Experimental analysis of photovoltaic integration with a proton exchange membrane electrolysis system for power-to-gas. Int J Hydrog Energy 2017;42:30569–83. https://doi.org/10.1016/j.ijhydene.2017.10.170.
[27] Ursua A, Gandia LM, Sanchis P. Hydrogen production from water electrolysis: current status and future trends. Proc IEEE 2012;100:410–26. https://doi.org/10.1109/JPROC.2011.2156750.
[28] Barbir F. PEM electrolysis for production of hydrogen from renewable energy sources. Sol Energy 2005;78:661–9. https://doi.org/10.1016/j.solener.2004.09.003.
[29] Riaz N, Sultan M, Miyazaki T, Shahzad MW, Farooq M, Sajjad U, et al. A review of recent advances in adsorption desalination technologies. Int Commun Heat Mass Transf 2021;128:105594. https://doi.org/10.1016/j.icheatmasstransfer.2021.105594.
[30] Swaminathan J, Tow EW, Stover RL, Lienhard JH. Practical aspects of batch RO design for energy-efficient seawater desalination. Desalination 2019;470:114097. https://doi.org/10.1016/j.desal.2019.114097.
[31] R. Singh, Emerging membrane technology for sustainable water treatment (Eds: N. P. Hankins, R. Singh), Elsevier, Boston, 2016.
[32] Kim J, Park K, Hong S. Application of two-stage reverse osmosis system for desalination of high-salinity and high-temperature seawater with improved stability and performance. Desalination 2020;492:114645. https://doi.org/10.1016/j.desal.2020.114645.
[33] Ni M, Leung MK, Leung DY. Electrochemistry modeling of proton exchange membrane (PEM) water electrolysis for hydrogen production. Proceeding WHEC 2006;16.
[34] Bernardi DM, Verbrugge MW. A mathematical model of the solid-polymer-electrolyte fuel cell. J Electrochem Soc 1992;139:2477. https://doi.org/10.1149/1.2221251.
[35] Chan SH, Xia ZT. Polarization effects in electrolyte/electrode-supported solid oxide fuel cells. J Appl Electrochem 2002;32:339–47. https://doi.org/10.1023/A:1015593326549.
[36] Thampan T, Malhotra S, Zhang J, Datta R. PEM fuel cell as a membrane reactor. Catal Today 2001;67:15–32. https://doi.org/10.1016/S0920-5861(01)00278-4.
[37] Gurau V, Barbir F, Liu H. An analytical solution of a half-cell model for PEM fuel cells. J Electrochem Soc 2000;147:2468–77.
[38] Espinosa-López M, Darras C, Poggi P, Glises R, Baucour P, Rakotondrainibe A, et al. Modelling and experimental validation of a 46 kW PEM high pressure water electrolyzer. Renew Energy 2018;119:160–73. https://doi.org/10.1016/j.renene.2017.11.081.
[39] Millet P, Andolfatto F, Durand R. Design and performance of a solid polymer electrolyte water electrolyzer. Int J Hydrog Energy 1996;21:87–93. https://doi.org/10.1016/0360-3199(95)00005-4.
[40] Ioroi T, Yasuda K, Siroma Z, Fujiwara N, Miyazaki Y. Thin film electrocatalyst layer for unitized regenerative polymer electrolyte fuel cells. J Power Sources 2002;112:583–7. https://doi.org/10.1016/S0378-7753(02)00466-4.
[41] Beattie PD, Basura VI, Holdcroft S. Temperature and pressure dependence of O2 reduction at Pt|Nafion® 117 and Pt|BAM® 407 interfaces. J Electroanal Chem 1999;468:180–92. https://doi.org/10.1016/S0022-0728(99)00164-3.
[42] Marković NM, Grgur BN, Ross PN. Temperature-dependent hydrogen electrochemistry on platinum low-index single-crystal surfaces in acid solutions. J Phys Chem B 1997;101:5405–13. https://doi.org/10.1021/jp970930d.
[43] Park K, Burlace L, Dhakal N, Mudgal A, Stewart NA, Davies PA. Design, modelling and optimisation of a batch reverse osmosis (RO) desalination system using a free piston for brackish water treatment. Desalination 2020;494:114625. https://doi.org/10.1016/j.desal.2020.114625.
[44] Darby R. Chem Eng Fluid Mech 2001.
[45] Wang Y-X, Ou K, Kim Y-B. Power source protection method for hybrid polymer electrolyte membrane fuel cell/lithium-ion battery system. Renew Energy 2017;111:381–91. https://doi.org/10.1016/j.renene.2017.03.088.
[46] Chen M, Rincon-Mora GA. Accurate electrical battery model capable of predicting runtime and I-V performance. IEEE Trans Energy Convers 2006;21:504–11. https://doi.org/10.1109/TEC.2006.874229.